JOURNAL OF SPACECRAFT AND ROCKETS
Vol. 36, No. 3, May–June 1999

Prediction and Validation of Mars Pathfinder Hypersonic Aerodynamic Database

Peter A. Gnoffo,* Robert D. Braun,† K. James Weilmuenster,* Robert A. Mitcheltree,‡
Walter C. Engelund,† and Richard W. Powell§
NASA Langley Research Center, Hampton, Virginia 23681-0001

Postflight analysis of the Mars Pathfinder hypersonic, continuum aerodynamic database is presented. Measured data include accelerations along the body axis and axis normal directions. Comparisons of preflight simulation and measurements show good agreement. The prediction of two static instabilities associated with movement of the sonic line from the shoulder to the nose and back was confirmed by measured normal accelerations. Reconstruction of atmospheric density during entry has an uncertainty directly proportional to the uncertainty in the predicted axial coefficient. The sensitivity of the moment coefficient to freestream density, kinetic models, and center-of-gravity location are examined to provide additional consistency checks of the simulation with flight data. The atmospheric density as derived from axial coefficient and measured axial accelerations falls within the range required for sonic line shift and static stability transition as independently determined from normal accelerations.

Nomenclature

A_A = axial acceleration, Earth g
A_N = normal acceleration, Earth g
C_A = axial force coefficient
C_D = drag coefficient
C_m = pitching moment coefficient
$C_{m,\alpha}$ = pitching moment coefficient derivative, per radian
C_N = normal force coefficient
D = probe diameter, m
h = altitude, km
M = Mach number
m = entry mass, kg
p = pressure, N/m^2
S = reference area, m^2
T_∞ = freestream temperature, K
V_∞ = freestream velocity, m/s
x, y, z = Cartesian coordinates, m
α = angle of attack, deg
α_T = total angle of attack, $(\alpha^2 + \beta^2)^{1/2}$, deg
β = angle of yaw, deg
γ = effective ratio of specific heats
ρ_∞ = freestream density, kg/m^3

Introduction

THE hypersonic aerodynamic database used in the Mars Pathfinder entry, descent, and landing (EDL) was predominantly generated using computational fluid dynamics. Whereas ground-based and flight data from the Viking project were used to check portions of the aerodynamic data for Pathfinder, differences in entry velocity and angle of attack between Pathfinder and Viking required a more critical evaluation of high-temperature effects on hypersonic aerodynamics. A systematic evaluation of Pathfinder aerodynamics as a function of velocity, altitude, and angle of attack in a continuum regime revealed two intervals during a nominal entry in which static aerodynamic instabilities would induce vehicle wobble. The static aerodynamic instability was associated with changing sonic line location and related pressure distributions as a function of chemical kinetics and flow energy. These predictions and explanations were described in 1996 (Refs. 1 and 2), and the wobble was confirmed by Pathfinder flight data (accelerometers) on July 4, 1997. The purpose of this paper is to critically review these predictions of Pathfinder aerodynamics in light of flight data. The physical phenomena leading to the static aerodynamic instability are reviewed, the measured accelerations confirming the instability are discussed, and additional postflight analyses are presented. The fidelity of comparison between preflight prediction and flight data significantly reduces uncertainty in the atmospheric reconstruction process and provides enhanced confidence in the application of computational fluid dynamics (CFD) to future planetary missions with reduced design margin.

Preflight Analysis

The Mars Pathfinder entry configuration is shown in Fig. 1. The forebody is a 70-deg half-angle cone with base diameter 2.65 m, nose radius 0.6638 m, and shoulder radius 0.06625 m. The on-axis reference point for aerodynamic moment coefficients is located 0.662 m behind the nose. The actual center-of-gravity (c.g.) location is (x_{cg}, y_{cg}, z_{cg}) = (0.000107, −0.000435, 0.71541), where z is distance behind the outer mold line of the nose and x and y are orthogonal to the body axis.

Predictions of a static aerodynamic instability for the Mars Pathfinder vehicle associated with shifting of the sonic line from the shoulder to the nose and back have been described in the literature.[1,2] Specific conclusions of Ref. 1 relating to the occurrence of the static aerodynamic instability on the 70-deg, spherically capped Pathfinder configuration are summarized as follows:

1) As the Mars Pathfinder probe descends through the Mars atmosphere, the minimum value of the postshock effective γ first decreases from frozen gas chemistry values to equilibrium values (1.094) corresponding to a velocity of 4.86 km/s. As the probe continues to decelerate through a near equilibrium postshock gas chemistry regime, the value of γ increases, until reaching its perfect gas value at parachute deployment (0.42 km/s).

2) For the spherically blunted, 70-deg half-angle cone at small angles of attack, the sonic line location shifts from the shoulder to the nose cap and back again on the leeside symmetry plane because of the change in γ. This transition in sonic line location is shown in Fig. 2 for a 2-deg angle of attack. The subsonic flow region, as

---

Received Feb. 10, 1998; presented as Paper 98-2445 at the AIAA/ASME 7th Joint Thermophysics and Heat Transfer Conference, Albuquerque, NM, June 15–18, 1998; revision received Aug. 5, 1998; accepted for publication Feb. 22, 1999. Copyright © 1999 by the American Institute of Aeronautics and Astronautics, Inc. No copyright is asserted in the United States under Title 17, U.S. Code. The U.S. Government has a royalty-free license to exercise all rights under the copyright claimed herein for Governmental purposes. All other rights are reserved by the copyright owner.

*Aerospace Engineer, Aerothermodynamics Branch, Aero and Gas Dynamics Division. Associate Fellow AIAA.

†Aerospace Engineer, Vehicle Analysis and Planetary Exploration Branch, Senior Member AIAA.

‡Aerospace Engineer, Aerothermodynamics Branch, Aero and Gas Dynamics Division. Senior Member AIAA.

§Aerospace Engineer, Vehicle Analysis and Planetary Exploration Branch, Associate Fellow AIAA.

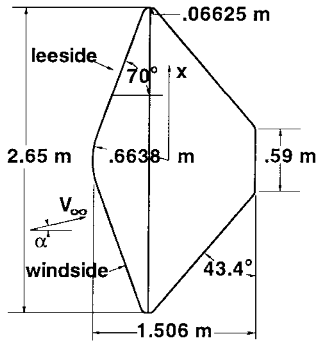

Fig. 1 Mars Pathfinder probe.

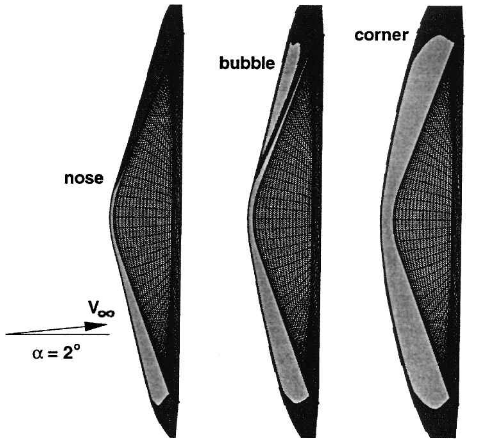

Fig. 2 Sonic line location over the Mars Pathfinder at 2-deg angle of attack and Mach numbers equal to 22.3 (left), 16.0 (center), and 9.4 (right) showing the effect of gas chemistry.

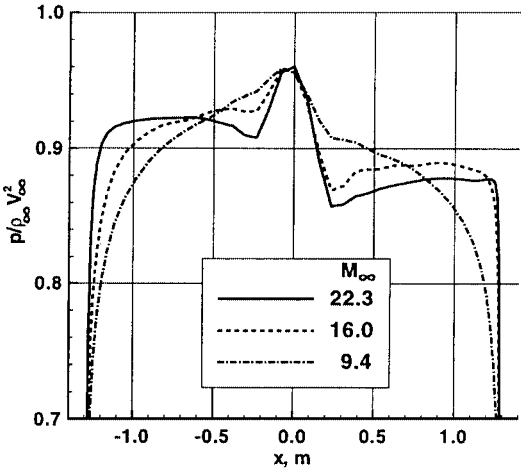

Fig. 3 Pressure distributions in the plane of symmetry over the Mars Pathfinder at 2-deg angle of attack and Mach numbers equal to 22.3, 16.0, and 9.4 showing the effect of gas chemistry.

defined by the frozen sound speed, appears as the light gray region. The darker region represents zones of supersonic flow behind the bow shock. At a Mach number 22.3 on the preflight Pathfinder simulation, the sonic line on the leeside dips deep into the boundary layer over the spherical nose cap. Later in the trajectory, at Mach 16.0, a subsonic bubble forms immediately behind the bow shock just downstream of an inflection point in the bow shock. The sonic line from the nose skirts above the edge of the boundary layer. Still later, at Mach 9.4, the bubble expands to merge with the subsonic region at the boundary-layer edge. The inflection point on the bow shock disappears.

3) Pressure distributions on the cone fustrum approaching the shoulder tend to be very flat when the sonic line sits forward over the spherical nose, as shown in Fig. 3 for Mach 22.3. Effects of the expansion over the shoulder can only be communicated upstream through the subsonic portion of the boundary layer. In contrast, pressure distributions on the cone fustrum approaching the shoulder tend to be more rounded when the sonic line sits on the shoulder, exhibiting a more pronounced influence of the expansion on the upstream flow as shown in Fig. 3 for Mach 9.4.

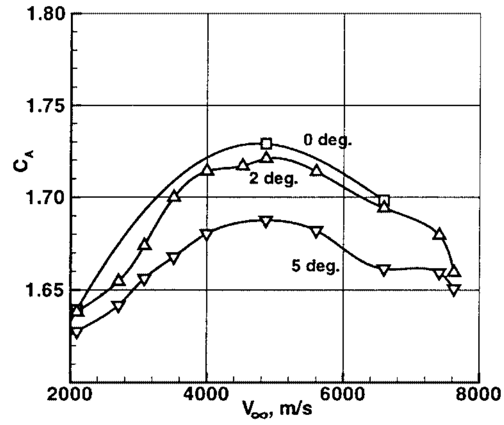

a) Axial coefficient

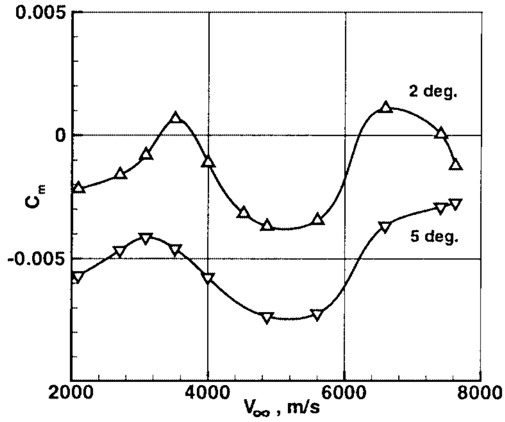

b) Pitching moment coefficient

Fig. 4 Predicted aerodynamic coefficients as function of velocity and angle of attack for early Mars Pathfinder trajectory with ballistic coefficient equal to 45.

4) In general, windside pressures exceed leeside pressures on the cone fustrum, producing a stabilizing moment that pitches the probe back to zero angle of attack. However, the behavior of the pressure distribution in the vicinity of the shoulder significantly influences the pitching moment coefficient because of the larger moment arms and surface area at the edge of the probe as compared to the inboard nose and fustrum regions. For the Mars Pathfinder probe at 2-deg angle of attack, the flat, leeside pressures approaching the shoulder (when the sonic line sits over the nose) can exceed the rounded windside pressures approaching the shoulder (when the sonic line sits over the shoulder). The net effect of this crossover distribution near the shoulder tends to pitch the probe to higher angles of attack (static instability). The overall balance (crossover-point location) is sensitive to freestream conditions and corresponding gas chemistry within the shock layer. The combination of small angle of attack, large cone angle, windside sonic line over the shoulder, and leeside sonic line over the nose with a secondary, subsonic zone above the leeside fustrum yield conditions that favor (but do not necessarily guarantee) a destabilizing pitching moment.

5) Representative parts of the aerodynamic database as a function of velocity during the hypersonic, continuum portion of the trajectory are shown in Fig. 4. Conditions for a positive, destabilizing moment coefficient derivative $C_{m,\alpha}$ occur twice in the Mars Pathfinder mission. (C_m is zero when α_T equals zero; $C_{m,\alpha}$ is positive where the C_m curve for $\alpha = 2$ deg crosses the $C_m = 0$ axis in Fig. 4b.) The first occurrence ($7.5 > V_\infty > 6.5$ km/s, $51 > h > 37$ km, vicinity of peak heating for this trajectory) results from the transition

in the sonic line location as a function of gas chemistry changing from nonequilibrium to equilibrium. The second occurrence ($4.0 > V_\infty > 3.1$ km/s, $25 > h > 22$ km) results from the transition in the sonic line location as a function of decreasing flow enthalpy in a near-equilibrium gas chemistry regime.

Measured Accelerations

Measured accelerations during Pathfinder's EDL validate these earlier conclusions. The raw, three-axis accelerometer data for the hypersonic portion of EDL are presented in Fig. 5. In Fig. 5, the z axis is in the axial direction. The x and y axes are fixed on the body as it spins (approximately 2 rpm), pitches, and precesses during descent. Peak dynamic pressure occurs approximately 78 s after entry interface. In the vicinity of peak dynamic pressure, the magnitude of the off-axis accelerations abruptly decreases, corresponding to a brief period where CFD simulations show the sonic line fixed to the spherical nose at small α_T.

The trend is more clearly observed in Fig. 6 in which a total normal acceleration $[A_N = (A_x^2 + A_y^2)^{1/2}]$ is plotted as a function of time. In Fig. 6, a rather abrupt increase in normal acceleration is observed on either side of the relative low level ($A_N \approx 0.014\,g$) near peak dynamic pressure to a relatively high level ($A_N \approx 0.04\,g$). This change closely corresponds to the predicted times when the sonic line shifts from the shoulder to the nose (≈71 s) and then back again to the shoulder (≈82 s).

In general, the correspondence of measured accelerations and predicted aerodynamic coefficients is complicated by the unknown freestream density. Velocity can be derived from integrated accelerations, but density is not directly measured. This complicating factor can be removed by examining the ratio of normal-to-axial forces and normal-to-axial aerodynamic coefficients:

$$\frac{C_N}{C_A} = \left(\frac{F_N}{\frac{1}{2}\rho_\infty V_\infty^2 S}\right)\Bigg/\left(\frac{F_A}{\frac{1}{2}\rho_\infty V_\infty^2 S}\right) = \frac{mA_N}{mA_A} = \frac{A_N}{A_A} \qquad (1)$$

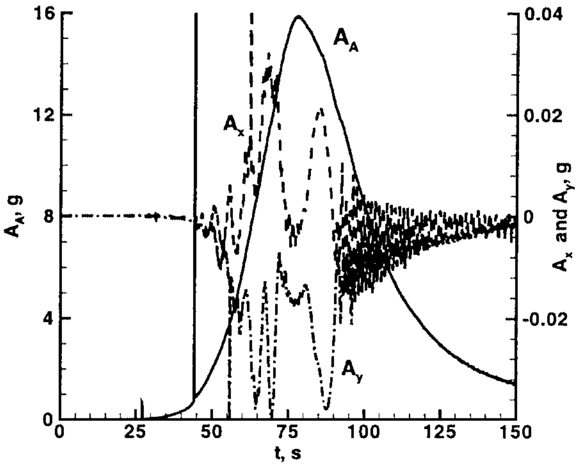

Fig. 5 Science accelerometer measurements recorded on Mars Pathfinder during 2.5 min following entry interface with the Mars atmosphere.

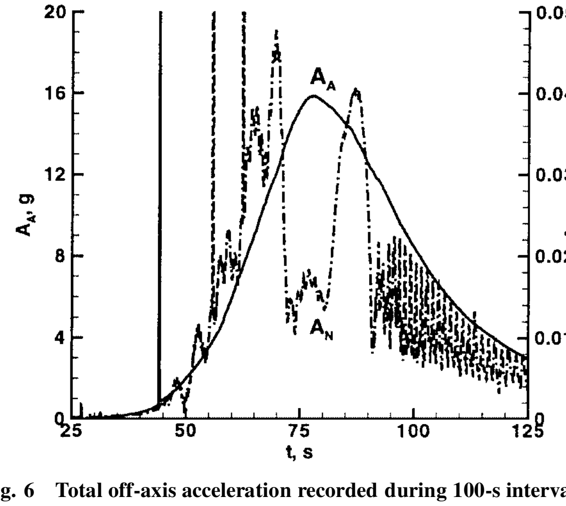

Fig. 6 Total off-axis acceleration recorded during 100-s interval surrounding peak dynamic pressure.

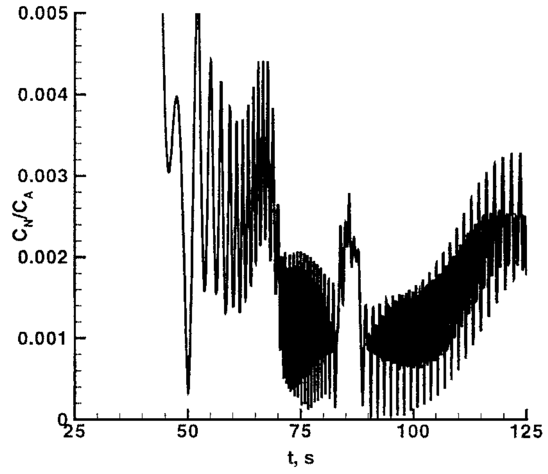

a) Predicted ratio of normal-to-axial force coefficients from six-DOF POST

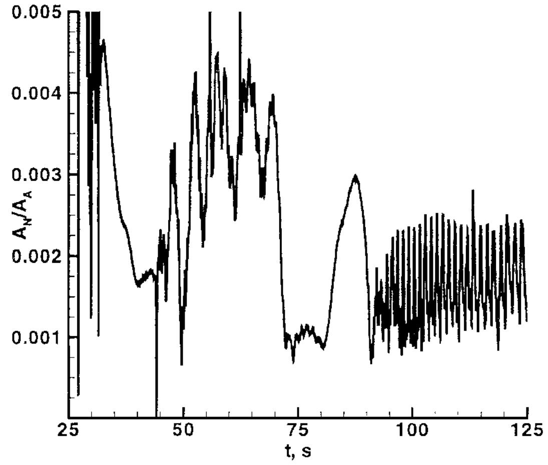

b) Measured normal-to-axial acceleration ratio

Fig. 7 Ratio of normal acceleration to axial acceleration recorded during 100-s interval surrounding peak dynamic pressure; ratio is equivalent to the value of C_N/C_A for Pathfinder at its total angle of attack α_T.

The predicted values of normal-to-axial force coefficients using the initial state vector determined 4 h prior to entry interface in the six-degree-of-freedom (DOF) POST[3] code and aerodynamic coefficient tables derived from CFD simulations,[1] are presented in Fig. 7a. The corresponding measured values of normal-to-axial accelerations are presented in Fig. 7b. The predicted and measured results show very good qualitative and quantitative agreement. For example, the effects of the predicted and measured static aerodynamic instability between 82 and 90 s are evident in both the magnitude and duration of the pulse. The time-averaged aerodynamic coefficient ratio in the vicinty of peak dynamic pressure between 71 and 82 s is also in good agreement with magnitude and duration of the measured ratio of accelerations when the sonic line sits over the spherical nose. The predictions show a much larger oscillation about the mean in this domain than was measured. An overly conservative specification for $C_{m,q}$ in this region in the simulation is the suspected cause. The magnitude and frequency of oscillations beyond 90 s are in fair agreement, but the mean value of measured acceleration ratio (0.0016) remains at a constant level whereas the mean value of the simulated acceleration ratio starts lower (0.0008) and gradually rises to 0.0024. Reasons for these discrepancies are not yet understood.

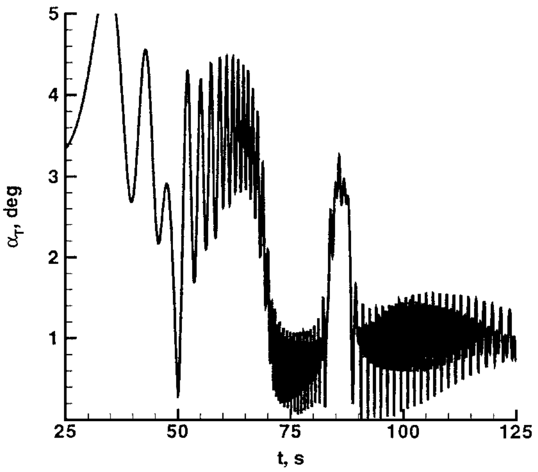

a) Predicted α_T from six-DOF POST

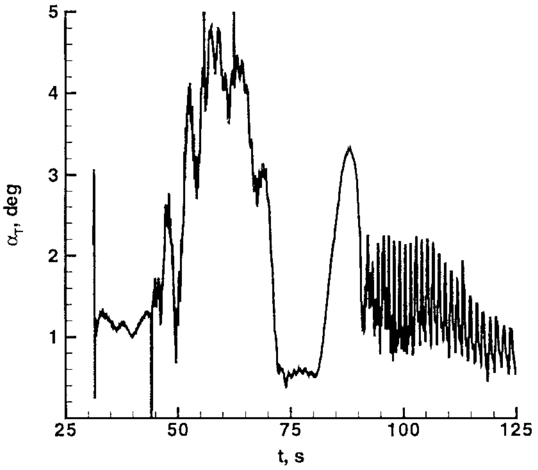

b) Derived α_T from recorded accelerations

Fig. 8 Comparison of total angle of attack α_T predicted by six-DOF POST using initial state vector determined 4 h prior to entry interface with values derived from measured accelerations.

The total angle of attack α_T predicted in the six-DOF POST analysis is presented in Fig. 8a. The corresponding values in flight (Fig. 8b) are derived from aerodynamic tables of C_N/C_A as a function of α_T using the measured ratio of normal-to-axial accelerations. Here again, both qualitative and quantitative agreement are generally good and serve to validate the simulation methodology for aerodynamics.

Atmospheric Reconstruction

Reconstruction of the Mars atmosphere based on measured accelerations on Mars Pathfinder has been described by Spencer et al.[4] Velocities are derived from measured accelerations. Densities are derived from measured axial accelerations, the derived velocities, and the predicted aerodynamic database for C_A as a function of velocity, Mach number, and total angle of attack. The point-by-point transformation is given by

$$\rho_\infty = \frac{2A_A}{V_\infty^2 C_A(S/m)} \tag{2}$$

Errors in the predicted aerodynamic database are linearly related to errors in the derived densities. The reconstructed density is plotted as a function of velocity in Fig. 9. The off-axis accelerations are plotted in Fig. 9 to show the correspondence of simulation coordinates (velocity, density) with the onset and decay of the aerodynamic instabilities at small angles of attack.

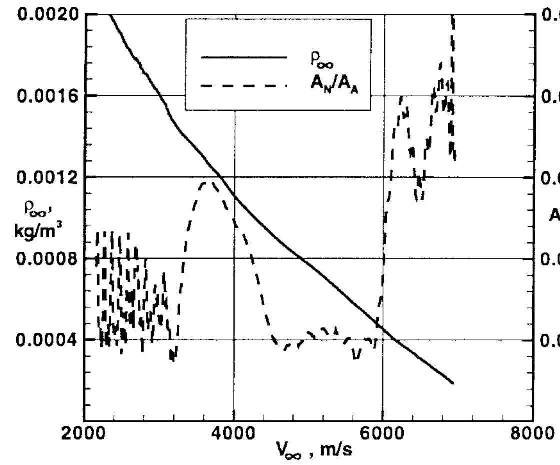

Fig. 9 Reconstructed density and ratio of measured accelerations as function of velocity for Mars Pathfinder during flight through the continuum, hypersonic flow regime.

Uncertainty Analysis

The uncertainty in c.g. location is ±5 mm in the axial and ±1 mm in the radial directions. Given $C_A \approx 1.7$ over the hypersonic, continuum portion of the trajectory, the uncertainty in C_m associated with the uncertainty of the c.g. location in the pitch plane is $\Delta C_m = C_A \Delta r/D = \pm 0.00064$. The uncertainty in C_m associated with an axial translation of the c.g. is two orders of magnitude smaller for small angles of attack. Note that there is no uncertainty in the aerodynamic reference point; we simply treat c.g. location uncertainty as equivalent to a corresponding change in the reference location.

All of the solutions generated for the next section and most of the solutions used to generate the aerodynamic database were obtained on a surface grid of 30 × 60 cells (half-body to symmetry plane) with 64 cells normal to the body. A grid refinement to 40 × 80 cells for a case with $V_\infty = 3515$ m/s at $\alpha = 2$ deg yielded a change in C_N/C_A of less than 0.00015, so that the predicted ratio of normal-to-axial acceleration has an uncertainty of at least ±0.00015. The change in C_m for this refinement was less than 0.0004. In a related grid coarsening test, the solution at the 6000 m/s and $\alpha = 2$ deg was computed on a grid with every other mesh point removed in all three computational directions. This test yielded a change in C_N/C_A of less than 0.00012 and a change in C_m less than 0.0003.

Measured axial accelerations in the hypersonic, continuum domain are accurate to within 1%. Uncertainties in measured normal accelerations are more difficult to characterize; they are expected to be less than 1% of full scale ($\Delta A_N < 0.008\,g$) in this domain. Velocities are derived by integrating the measured accelerations in time from the initial state vector. Uncertainties in the derived velocities should be less than 1% because random errors in measured accelerations smooth out and calibration checks remove bias errors in measured accelerations. Furthermore, an independent check of derived velocity with altimeter data prior to parachute deployment showed differences less than 1%.

Uncertainties in the derived density are linearly related to the total uncertainty in the simulated values C_A, which include uncertainties associated with α_T and gas chemistry model [recall Eq. (2)]. Uncertainties in the derived density are quadratically related to the total uncertainty in freestream velocity. Comparison of LAURA simulations to ground-based experimental data for an axisymmetric blunt body (METEOR[5]) at Mach 6 in which uncertainties in gas chemistry (perfect gas) and α_T (sting mounted) are near zero (relative to the flight case) show differences less than 2% in C_A and less than 5% in C_N and C_m. Uncertainty in C_A associated with the gas model is difficult to define, but thought to be approximately 1% for low angles of attack based on computational analysis in the next section. Uncertainty in the derived α_T is implicitly related to the uncertainty in C_N and measured accelerations; given the values discussed earlier and the tables and figures from the preflight analysis,[1] the uncertainty in α_T should be less than 0.6 deg. The uncertainty in C_A due to the uncertainty in α_T is less than 0.7%. Effects of base pressure on the hypersonic aerodynamic drag are less than 0.5% (Ref. 1). Consequently, the total rms value for uncertainty in C_A in the hypersonic, continuum domain at low angles of attack is less than 3%. The corresponding total rms value for uncertainty in ρ_∞ in this domain is less than 4%. Comparisons of computed drag coefficient[1] to experimental data[6] for the Viking configuration in ballistic range tests in CO_2 fall within this 3% estimate.

As a final note, all of the simulations assume laminar flow. The assumption should be valid for most of the hypersonic, continuum trajectory presented here. At the $V_\infty = 3996$ m/s trajectory point ($M_\infty = 18$, $Re_{D,\infty} = 1.2 \times 10^6$), the value of Re_θ / M_e is less than 500 over most of the cone and drops below zero as flow expands over the shoulder. In recent comparisons to engineering code assessments of Re_θ / M_e, the CFD valuation of this quantity is roughly twice the engineering code valuation. Assuming a transition criterion of $Re_\theta / M_e = 250$ for blunt bodies from engineering code assessments, turbulent flow may occur near this condition. The contribution of laminar skin friction to C_A is less than 0.2%, as noted in block 2 of Table 4 ($M_\infty = 16$, $V_\infty = 3515$ m/s, $\alpha = 2$ deg) in the preflight analysis of Ref. 1. If we assume 1) no relaminarization at the shoulder where the strongest contribution of shear to C_A will occur, 2) negligible displacement thickness effects of a turbulent boundary layer on pressure for this very blunt configuration, and 3) a factor five increase in shear over laminar values, then an additional uncertainty of 1% in C_A is introduced. The contribution from turbulent shear at the shoulder to C_m at small angles of attack is more difficult to estimate because of the greater importance of differences between windside shoulder and leeside shoulder contributions. The laminar shear contribution to C_m for the $M_\infty = 16$ simulation noted earlier is a destabilizing increment equal to 0.00012. Again assuming a factor five increase in the turbulent contribution leads to an additional uncertainty in C_m equal to 0.0006.

Sensitivity Analysis

The aerodynamic database used in the POST code was originally generated on the basis of a simulated trajectory for a 418-kg vehicle with a ballistic coefficient of 45 kg/m^2 in the MarsGRAM atmospheric model.[7] The vehicle grew as the design matured, and the actual entry mass was 585.3 kg, with a ballistic coefficient of 62 kg/m^2. In the final design phase, cruise and entry operations, and postflight analysis, the Clancy et al.[8] atmospheric model (also see Ref. 9) was used. The POST code used velocity as a curve-fit parameter for aerodynamic coefficients above Mach 12 in the continuum regime because of the important role of effective γ on aerodynamics and its dependence on total enthalpy. Below Mach 8, Mach number was used as a correlating parameter to emphasize compressibility effects on aerodynamics. Between Mach 8 and 12, a bridging function is used. As a result of differences in mass, entry angle, and atmospheric model, a comparison of the early preflight and postflight trajectories will yield different densities for the same velocity. As a point of reference, the database used aerodynamic coefficients simulated at $V_\infty = 3996$ m/s and $\rho_\infty = 1.55 \times 10^{-3}$ kg/m^3; the density at that same velocity in the reconstructed atmosphere was $\rho_\infty = 1.13 \times 10^{-3}$ kg/m^3.

In the continuum, hypersonic flight regime, the change in density would be expected to influence aerodynamic coefficients through Reynolds number and gas kinetics. As discussed in the preceding section, the influence of Reynolds number is expected to be small, but the influence of gas kinetics on the effective γ is unknown. The primary purpose of this section is to quantify the sensitivity of the aerodynamic database to perturbations in density and the gas kinetic model. A secondary purpose of this section is to critically evaluate the transition regions between statically stable and unstable regions and check that the simulation is consistent with measured normal accelerations.

The moment coefficient at $\alpha = 2$ deg for the postflight, simulated trajectory is plotted over the simulated Pathfinder measurements of normal-to-axial acceleration as a function of velocity in Fig. 10. The value of C_m at $\alpha = 2$ deg, designated $C_m(2)$, is proportional to $C_{m,\alpha}$ at $\alpha = 0$ assuming a forward difference approximation: $C_{m,\alpha}(0) = [C_m(2) - 0] \times 90/\pi$. The purpose of Fig. 10 is to identify values of $C_m(2)$ that are associated with the transition between regions of static instability and static stability. The transition region is delineated by the rectangles.

Table 1 Test points and baseline aerodynamics

Point	V_∞, m/s	ρ_∞, kg/m^3	$C_A(2)$	$C_N(2)$	$C_m(2)$
A	6000	4.53×10^{-4}	1.707	0.004399	−0.001292
B	4270	1.00×10^{-3}	1.714	0.004394	−0.001929
C	3996	1.13×10^{-3}	1.712	0.003250	−0.000812
D	3648	1.26×10^{-3}	1.698	0.001883	+0.000331

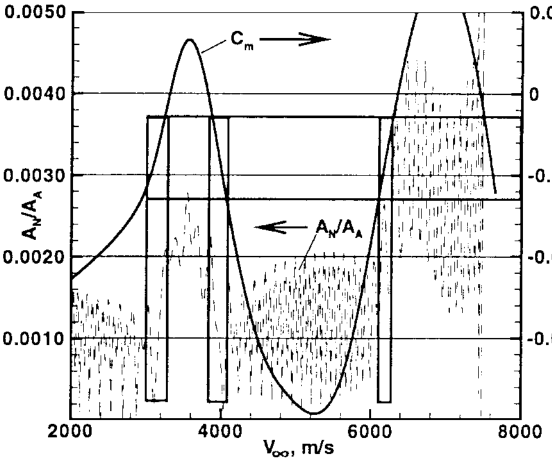

Fig. 10 Ratio of normal to axial accelerations and moment coefficient at $\alpha = 2$ deg for the preflight simulated trajectory as a function of velocity; transition between regions of static instability and static stability are bounded with the rectangular boxes.

We introduce an assumption that critical values in $C_m(2)$ may be defined that serve to delineate the various stability regions as determined from measured accelerations. In each transition region, an upper limit on $C_m(2)$, $C_{m,U}$ is identified such that any simulation with $C_m(2) > C_{m,U}$ would be expected to be in a region of static instability. In like manner, a lower limit on $C_m(2)$, $C_{m,L}$ is identified such that any simulation with $C_m(2) < C_{m,L}$ would be expected to be in a region of static stability. If $C_{m,U} > C_m(2) > C_{m,L}$, one would expect measured accelerations to be within the transition between the two stability regions.

Values of $C_{m,U}$ and $C_{m,L}$ are obtained from analysis of four different simulations of the Pathfinder trajectory through the reconstructed atmosphere. The vehicle was numerically flown using the six-DOF POST code with the baseline aerodynamic database and three perturbations in which the curve fits of aerodynamic coefficients as a function of velocity were shifted by +1, −5, and −10% in velocity space, i.e., $C_x = C_x(V_\infty - 0.1V_\infty)$. This shift causes the instabilities to arise earlier or later in the simulated trajectory and allows us to check the assumption that critical values for $C_{m,U}$ and $C_{m,L}$ can be defined. Values for $C_{m,U}$ and $C_{m,L}$ based on this subjective selection criterion are, respectively, −0.0003 and −0.0013 (see bounding boxes in Fig. 10). When the major contributor to uncertainty in C_m, c.g. location is included, the transition range expands to +0.00034 to −0.00194.

Results and Discussion

Four test points are chosen along the reconstructed trajectory and are identified in Table 1 and in Fig. 11. The simulated data in Fig. 11 are based on flight through the reconstructed atmosphere, in contrast to the data in Fig. 7a based on flight through the preflight atmospheric model. Except for the lack of high-frequency oscillations in the measured data between 3400 and 6000 m/s, there is fairly good qualitative agreement between the measured and simulated data. (Temporal resolution of the accelerometers should have picked up such oscillations if they were present.) The magnitude of measured accelerations is slightly larger (15–30%) than the temporally averaged level of simulations in the statically stable region between 4500 and 6000 m/s and in the statically unstable region between 3400 and 4000 m/s. The measured duration of the statically stable region in velocity space is shorter than the simulated duration. These observations are consistent with trends shown in

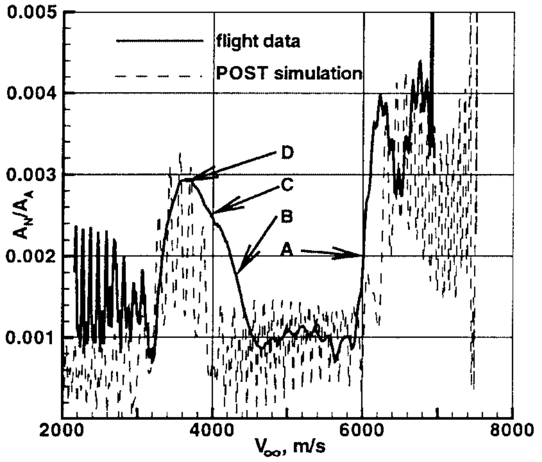

Fig. 11 Comparison of A_N/A_A as measured in flight and as simulated with the POST code in the reconstructed atmosphere using the CFD-derived database for aerodynamic coefficients.

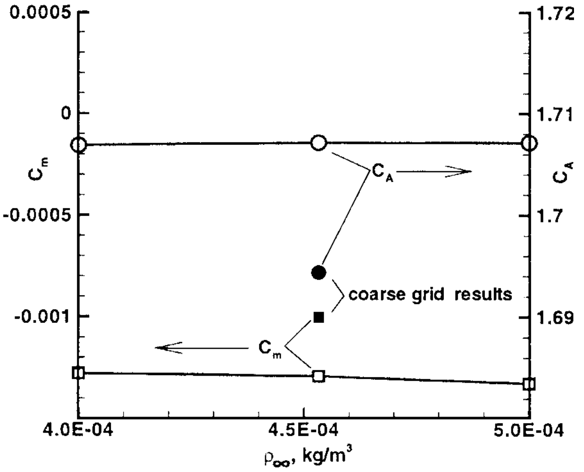

Fig. 12 Computed sensitivity of Pathfinder aerodynamic coefficients on freestream density for a velocity of 6000 km/s.

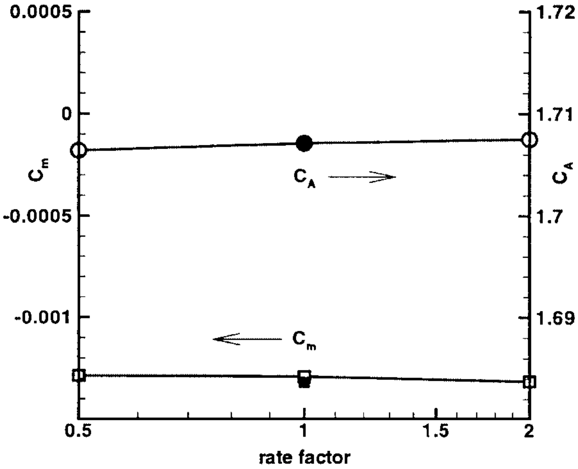

Fig. 13 Computed sensitivity of Pathfinder aerodynamic coefficients on dissociation rate coefficient for CO_2 at a freestream density of 0.0004532 kg/m^3 and velocity of 6000 km/s.

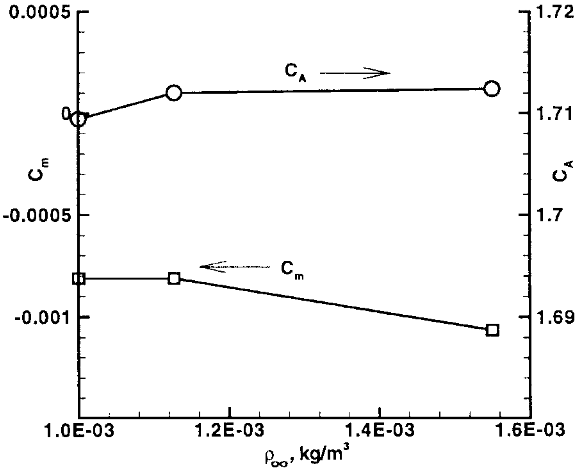

Fig. 14 Computed sensitivity of Pathfinder aerodynamic coefficients on freestream density for a velocity of 3996 km/s.

Fig. 9 of Braun et al.[2] in which the c.g. moves off the axis. The current simulation assumes a 0.448-mm offset c.g. location.

The aerodynamic coefficients for the baseline eight-species (CO_2, CO, N_2, O_2, NO, C, N, and O) kinetic model[10] are included in Table 1. Point A is in the middle of the transition region, near peak heating and prior to peak dynamic pressure, where the sonic line is completing its movement to the nose with decreasing γ. Point B is in the middle of the next transition, after peak dynamic pressure in which the sonic line is beginning to move back to the shoulder from the nose with increasing γ associated with decreasing flow enthalpy. At this point in Fig. 11, the POST simulation indicates a region of static stability, in apparent disagreement with the flight data. Point C is at the end of this transition region containing point B; the velocity here corresponds to one used in establishing the aerodynamic database. Point D is at the local maximum for A_N/A_A.

Given the assumptions stated earlier, values of $C_m(2)$ for points A–C would be expected to be between $C_{m,U}$ and $C_{m,L}$. The value of $C_m(2)$ for point D would be expected to be greater than $C_{m,U}$. As is evident in Table 1, the baseline kinetic model yields values of $C_m(2)$ that are consistent with the critical values of $C_{m,U}$ and $C_{m,L}$ for points A, C, and D, even without adding the uncertainty bar associated with c.g. location. The uncertainty bar around point B associated with c.g. location just overlaps the lower limit for $C_{m,L}$ that defines the transition region.

The sensitivity of $C_A(2)$ and $C_m(2)$ with respect to ρ_∞ and the kinetic model at point A are shown in Figs. 12 and 13, respectively. Open symbols represent the baseline grid results (60 × 30 × 64), and the filled symbols show a result with a factor two coarsening in all coordinate directions. Aerodynamic coefficients are insensitive to perturbations as large as 10% about the nominal density of 4.53×10^{-4} kg/m^3. The value for $C_m(2)$ at point A is at the lower edge of the expected transition range. Aerodynamic coefficients are also insensitive to changes in the dissociation rate constant for CO_2 by factors varying from 0.5 to 2.0. Inspection of CO_2 mass fraction in all three solutions shows that CO_2 is substantially depleted; other species play a more dominant role in establishing γ. Changing the effective temperature for dissociation in all such reactions at point A from the baseline model ($T_{\mathrm{eff}} = T^{0.5}T_V^{0.5}$; open symbols) to $T_{\mathrm{eff}} = T^{0.7}T_V^{0.3}$ (filled symbols) has almost no effect. Whereas thermal nonequilibrium is present in the shock layer, there is not enough thermal nonequilibrium over substantial portions of the shock layer to make a significant effect on aerodynamics through effective kinetic rates.

The sensitivity of $C_A(2)$ and $C_m(2)$ with respect to ρ_∞ and the kinetic model at point C are shown in Figs. 14 and 15, respectively. Aerodynamic coefficients are still insensitive to perturbations as large as 40% about the nominal density of 1.13×10^{-3} kg/m^3. In contrast, the effect on $C_m(2)$ of a 7% perturbation in velocity at the same density is large, as observed by comparing point B in Table 1 with the result for ρ_∞ equal to 0.001 kg/m^3 in Fig. 14. The effect of dissociation rate constant for CO_2 on aerodynamics is stronger at point C than at point A. Previous characterization of the flow at this point as near equilibrium oversimplified the role of gas kinetics during this portion of the trajectory. Doubling the rate factor moves $C_m(2)$ closer to a predicted domain of static stability. Reducing the rate by a factor of 10 moves $C_m(2)$ closer to a predicted domain of static instability. Nevertheless, the change in $C_A(2)$ over this entire range of kinetic model adjustments is less than 0.6%.

The movement of the sonic line associated with changes in the CO_2 dissociation rate at point C are shown in Fig. 16. The baseline

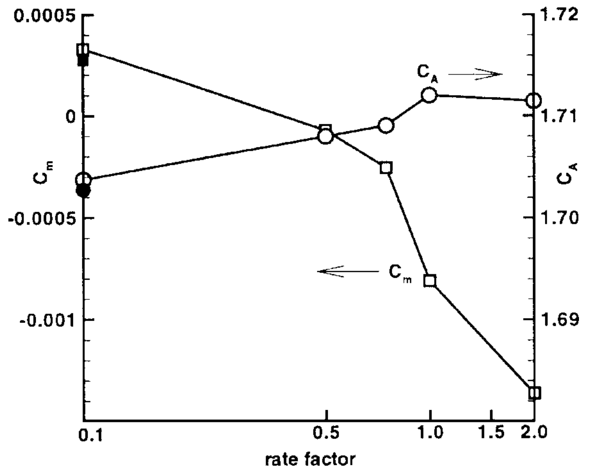

Fig. 15 Computed sensitivity of Pathfinder aerodynamic coefficients on dissociation rate coefficient for CO_2 at a freestream density of 0.001127 kg/m^3 and velocity of 3996 km/s.

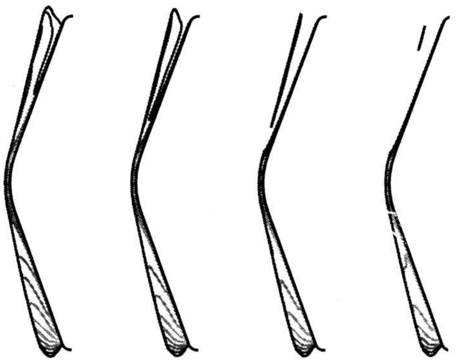

(a) 0.1 (b) 0.5 (c) 1.0 (d) 2.0

Fig. 16 Computed sensitivity of Pathfinder sonic line location on dissociation rate coefficient for CO_2 at a freestream density of 0.001127 kg/m^3 and velocity of 3996 km/s.

kinetic model results are in Fig. 16c, with rate factor equal to 1. Increasing rate factor causes the sonic bubble to shrink and the moment coefficient to move into the domain of static stability. Decreasing rate factor causes the sonic bubble to grow and approach a condition of static instability. The sonic bubble emanates from an inflection point in the bow shock, which eventually disappears with the merging of the bubble with the sonic line on the edge of the boundary layer.

The sensitivity tests at points A and C show that aerodynamic database is insensitive to perturbations in density as large as 10%. It is believed this lack of sensitivity would persist across the entire hypersonic, continuum domain for the Pathfinder vehicle shape. The sensitivity will manifest itself during the transitional flow regime prior to continuum; in fact, Moss et al.[11] predicted static instabilities in the transitional regime for Pathfinder as a function of Knudsen number variation.

The baseline thermochemical model yields values for $C_m(2)$ that are consistent, within estimated uncertainty bands, of the measured normal accelerations. Point B shows the greatest disagreement between measurement and simulation of normal accelerations. Agreement would likely be improved using a simulation with a larger offset c.g. and/or slower CO_2 dissociation rates to define C_m.

The normal acceleration data are useful as a consistency check for the simulation models, much like measurements of shock standoff distance in ground-based experiments are used. Whereas one could not use the data by itself to propose changes to any element(s) of the chemical kinetic model, one should question any model changes that cause inconsistent values of $C_m(2)$ with measured normal accelerations along any point on the Pathfinder trajectory. In the tests conducted herein, rather large perturbations in the kinetic model are required before computed values for $C_m(2)$ are pushed outside of the expected limits based on measured normal accelerations.

Conclusions

Predictions of two regions of static instability during the hypersonic, continuum portion of the Mars Pathfinder trajectory are verified by flight measurements of normal accelerations. The relation of these instabilities to sonic line movement between the nose and the shoulder as a function of trajectory point and kinetic model is demonstrated using numerical simulation of the flowfield in thermochemical nonequilibrium.

Perturbations to density as large as 10% about nominal values for the reconstructed trajectory during the hypersonic, continuum regime cause negligible change (less than 1%) in C_A. Large changes in the kinetic model in this regime cause changes in C_A of approximately 1%. Given other sources of uncertainty unrelated to the simulation model, the reconstructed density, with uncertainty linearly related to uncertainty in C_A, is expected to have approximately 4% uncertainty in the hypersonic, continuum regime.

The occurrence of static instabilities as recorded by normal accelerations during the Mars Pathfinder EDL provide an opportunity for CFD code validation. Computed moment coefficients are consistent with identified ranges for measured normal accelerations indicating flight in a statically stable or unstable regime. The definitions of these ranges for C_m are independent of CFD simulation; they are extracted from six-DOF trajectory simulations using several aerodynamic coefficient models for flight through the Mars atmosphere. The present simulations are consistent with measured data within the defined ranges, including the uncertainty band.

Acknowledgment

The authors thank Robert Blanchard of the Aerothermodynamics Branch, NASA Langley Research Center, for supplying data for the reconstructed atmosphere, trajectories, and accelerometers.

References

[1] Gnoffo, P. A., Weilmuenster, K. J., Braun, R. D., and Cruz, C. I., "Influence of Sonic-Line Location on Mars Pathfinder Probe Aerothermodynamics," *Journal of Spacecraft and Rockets*, Vol. 33, No. 2, 1996, pp. 169–177.

[2] Braun, R. D., Powell, R. W., Cruz, C. I., Gnoffo, P. A., and Weilmuenster, K. J., "Six Degree-of-Freedom Atmospheric Entry Analysis for the Mars Pathfinder Mission," AIAA Paper 95-0456, Jan. 1995.

[3] Brauer, G. L., Cornick, D. E., and Stevenson, R., "Capabilities and Applications of the Program to Optimize Simulated Trajectories (POST)," NASA CR-2770, Feb. 1977.

[4] Spencer, D. A., Thurman, S. W., Peng, C.-Y., Blanchard, R. C., and Braun, R. D., "Mars Pathfinder Atmospheric Entry Reconstruction," American Astronautical Society, AAS Paper 98-146, Feb. 1998.

[5] Gnoffo, P. A., Weilmuenster, K. J., Hamilton, H. H., II, Olynick, D. R., and Venkatapathy, E., "Computational Aerothermodynamic Design Issues for Hypersonic Vehicles," AIAA Paper 97-2473, June 1997.

[6] Intrieri, P. F., Rose, C. E. D., and Kirk, D. B., "Flight Characteristics of Probes in the Atmospheres of Mars, Venus and the Outer Planets," *Acta Astronautica*, Vol. 4, 1997, pp. 789–799.

[7] Justus, C. G., James, B. F., and Johnson, D. L., "Mars Global Reference Atmospheric Model (Mars-GRAM 3.3.4): Programmers Guide," NASA TM-108509, May 1996.

[8] Clancy, R., Lee, S., Gladstone, G., McMillan, W., and Rousch, T., "A New Model of Mars Atmospheric Dust Based on Analysis of Ultraviolet Through Infrared Observations from Mariner-9, Viking, and Phobos," *Journal of Geophysical Research*, Vol. 100, 1995, pp. 5251–5263.

[9] Spencer, D., and Braun, R., "Mars Pathfinder Atmospheric Entry: Trajectory Design and Dispersion Analysis," *Journal of Spacecraft and Rockets*, Vol. 33, No. 5, 1996, pp. 670–676.

[10] Mitcheltree, R. A., "Aerothermodynamic Methods for a Mars Environmental Survey Mars Entry," *Journal of Spacecraft and Rockets*, Vol. 31, No. 3, 1994, pp. 516–523.

[11] Moss, J. N., Wilmoth, R. G., and Price, J. M., "DSMC Simulations of Blunt Body Flows for Mars Entries: Mars Pathfinder and Mars Microprobe Capsules," AIAA Paper 97-2508, June 1997.

R. D. Braun
Guest Editor